Computers, Materials & Continua

Tech Science Press

Doi:10.32604/cmc.2025.069709

ARTICLE

A New Quadrilateral Finite Element Formulation for the Free Vibration Analysis of CNT-Reinforced Plates with Cutouts

Boudjema Bendaho[1], **Abdelhak Mesbah**[1] **and Zakaria Belabed**[1,2,*]

[1]Department of Civil Engineering & Public Works, Institute of Technology, Naama University Center, BP 66, Naama, 45000, Algeria
[2]Artificial Intelligence Laboratory for Mechanical and Civil Structures and Soil, Institute of Technology, Naama University Center, BP 66, Naama, 45000, Algeria

*Corresponding Author: Zakaria Belabed. Email: belabed@cuniv-naama.dz

Received: 29 June 2025; Accepted: 22 August 2025; Published: 23 September 2025

ABSTRACT: A new quadrilateral finite element IQ4 is developed for the free vibration of carbon nanotube-reinforced composite (CNTRC) perforated plates with a central cutout. By enriching the membrane part and incorporating a projected shear technique, the IQ4 element is proposed to address the known limitations of the standard Q4 element, such as shear locking and limited consistency in the coupling of membrane-bending components. The proposed element is formulated within the FSDT-based framework and assessed through benchmark tests to verify its convergence and accuracy. The governing equations are obtained via the weak form of Hamilton's principle. Particular attention is given to the influence of carbon nanotube volume fraction, distribution patterns, and boundary conditions on the fundamental frequency response of CNTRC plates with cutouts. In addition, a parametric study is conducted to assess the influence of cutout geometric configuration, shape, and size ratios on the vibrational response of the CNTRC plate. The numerical results demonstrate that the formulated IQ4 element provides stable and accurate estimations of natural frequencies, even in the presence of a cutout and the coupled effects of the non-uniform distribution of reinforcement through the plate thickness. The developed formulation is expected to contribute to the structural design and optimization of advanced lightweight systems, particularly in aerospace and mechanical engineering applications.

KEYWORDS: Free vibration analysis; improved quadrilateral element (IQ4); projected shear technique; membrane enrichment; cutout; carbon nanotube-reinforced composites (CNTRC)

1 Introduction

In recent years, carbon nanotube-reinforced composite (CNTRC) structures have received increasing attention due to the exceptional mechanical, thermal, and vibrational properties imparted by carbon nanotubes (CNTs) embedded within polymer matrices [1–4]. Numerical and experimental results in the literature consistently indicate that a low volume fraction of CNT reinforcements contributes notably to the mechanical enhancement of nanocomposite plates [5,6]. As a result, CNT-based composites are now being considered for critical applications in aerospace, mechanical, and civil engineering, where lightweight and high-performance materials are essential. Extensive research has been devoted to plates containing geometric discontinuities, including cutouts, which serve practical purposes such as weight reduction and access provision [7–9]. However, it is now well established that these discontinuities significantly affect changes in the global dynamic characteristics and the local stress distribution [10,11]. The mechanical impact of cutouts manifests in elevated stress zones and reduced local rigidity, leading to abrupt deformation gradients, which are more severe in CNT-reinforced composites due to their anisotropy and functional gradation of

constituents [12–15]. Various cutout shapes, such as circular, elliptical, and polygonal openings, influence nanocomposites' vibrational and stability behavior and functionally graded plates, and have been extensively investigated [16–19]. A common framework adopted in earlier studies involves the application of classical or first-order shear deformation plate theories, integrated with Ritz-based solutions using polynomial or Chebyshev expansions [20–22]. Although these approaches offer fundamental insights, their predictive accuracy tends to degrade in regions exhibiting steep strain gradients near cutouts and under different boundary conditions. Moreover, conventional low-order finite elements frequently encounter numerical artifacts, including shear locking and sensitivity to mesh refinement near cutout regions [23–25]. Several advanced theories have emerged to address these challenges: higher-order deformation kinematics, nonlocal and gradient-enhanced elasticity, and NURBS-based isogeometric approaches [26–29]. Nonetheless, the practical application of these techniques remains constrained by their intensive computational requirements and complex formulation procedures [30–32]. In addition, several of these approaches are unsuited for capturing the interaction between perforation shape, material gradation patterns, and mechanical modeling strategy. Recent research has increasingly turned toward the detailed analysis of advanced composite structures, with particular attention given to functionally graded carbon nanotube-reinforced composites and porous materials featuring intricate cutouts. Several analytical models have been proposed to explore their vibration and damping behaviors; many utilize higher-order shear deformation theory, various energy-based approaches, and the Rayleigh–Ritz method. These models have proven effective in capturing the dynamic response of CNT-reinforced plates embedded with viscoelastic layers. In parallel, bending behavior in FG-CNTRC panels has been assessed using shell elements derived from Kirchhoff–Love theory, integrating correction factors to reflect the efficiency of carbon nanotube reinforcement. Porous solids with irregular cutout shapes have been examined on a structural complexity front using three-dimensional elasticity formulations and hybrid Q4-T4 finite element meshes [33–37]. These studies highlight the impact of porosity distribution and cutout geometry on the system's natural frequencies. Experimental investigations have also contributed to the field. Notably, tests conducted on honeycomb sandwich beams under clamped-free boundary conditions have offered valuable insights into vibrational behavior, particularly with core structure and fundamental damping mechanisms. In light of these challenges, a new quadrilateral finite element is presented to investigate the free vibration behavior of CNTRC plates with cutouts. The formulation is founded in first-order shear deformation theory (FSDT) and incorporates refined membrane and shear components interpolations to enhance numerical accuracy. This enrichment allows for accurately modeling strain gradients near the cutout region and effectively avoids shear locking without requiring refined meshes or higher interpolation functions. The formulation accommodates both uniform and functionally graded CNT distributions using rule-of-mixtures micromechanical-based models. The performance of the proposed IQ4 element is assessed through a series of benchmark problems involving CNTRC plates both with and without cutouts, and the obtained results are compared against established reference solutions. The effects of cutout shape, size, CNT volume fraction, distribution patterns, boundary conditions, and plate geometry on the vibrational response are systematically investigated. The developed approach is well-positioned for integration into the structural optimization of lightweight, cutout-bearing components exposed to vibratory environments.

2 Problem Formulation

2.1 Mechanical Properties of CNTs Reinforced Plates

A functionally graded carbon nanotube-reinforced composite (FG-CNTRC) plate with a central rectangular cutout and a uniform thickness h is considered, as illustrated in Fig. 1. The Cartesian coordinate system (x, y, z) is defined such that the plane $z = 0$ coincides with the mid-surface of the plate. The rectangular cutout located at the center of the plate has side lengths c and d, representing its dimensions in the x- and y-directions, respectively. In Fig. 2, the FG-CNTRC plate is modeled as a two-phase nanocomposite of

aligned carbon nanotubes (CNTs) embedded in an isotropic polymer matrix. CNTs are continuously distributed through the thickness according to one of four patterns: UD (uniform distribution), FG-O (mid-plane concentration), FG-X (symmetric surface concentration), and FG-V (graded from top to bottom). These gradation schemes define the CNT volume fraction as a function of the thickness z-coordinate, designed to optimize the mechanical performance of the nanocomposite plate.

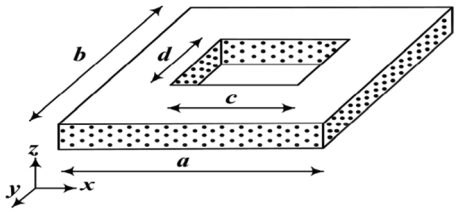

Figure 1: Geometrical configuration of a FG-CNTRC plate with a central rectangular cutout

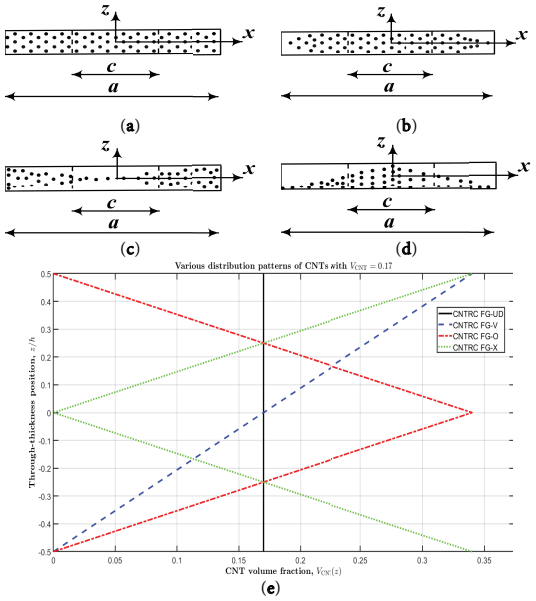

Figure 2: CNTs through the z-direction distribution patterns: (**a**) FG-UD; (**b**) FG-O; (**c**) FG-X; (**d**) FG-V; (**e**) z-thickness distribution patterns of CNT volume fraction $V_{CNTs}(z)$ for FG-CNTRC plates with V^{*}_{CNTs} = 0.17

The volume fraction of CNTs $V_{CNTs}(z)$ according to each distribution pattern, it is defined as follows [38,39]:

$$V_{CNTs}(z) = \begin{cases} V^{*}_{CNTs} & \text{for FG-UD} \\ V^{*}_{CNTs}\left(2 - \dfrac{4|z|}{h}\right) & \text{for FG-O} \\ V^{*}_{CNTs}\left(\dfrac{4|z|}{h}\right) & \text{for FG-X} \\ V^{*}_{CNTs}\left(1 + \dfrac{2z}{h}\right) & \text{for FG-A} \end{cases} \tag{1}$$

here, V^{*}_{CNTs} represents the intended amount of CNT reinforcement within the matrix material related to the distribution through the z-coordinate. The effective elastic properties, including Young's modulus $E(z)$, shear modulus $G(z)$, and mass density $\rho(z)$, are estimated using the rule of mixtures, as described [40,41]:

$$\begin{cases} E_{11}(z) = \eta_1 V_{CNTs}(z) E_{11}^{CNTs} + V_m(z) E_m \\ \frac{\eta_2}{E_{22}(z)} = \frac{V_{CNTs}(z)}{E_{22}^{CNTs}} + \frac{V_m(z)}{E_m} \\ \frac{\eta_3}{G_{12}(z)} = \frac{V_{CNTs}(z)}{G_{12}^{CNTs}} + \frac{V_m(z)}{G_m} \\ \rho(z) = V_{CNTs}(z) \rho_{CNTs} + V_m(z) \rho_m \end{cases} \tag{2}$$

For convenience, the volume fraction of the polymer matrix is assumed to be:

$$V_m(z) = 1 - V_{CNTs}(z) \tag{3}$$

here, E_{11}^{CNTs}, E_{22}^{CNTs} and G_{12}^{CNTs} denote the longitudinal and transverse Young's moduli and the shear modulus of the carbon nanotubes, respectively. While E_m and G_m represent the corresponding elastic properties of the polymer matrix. The coefficients η_1, η_2 and η_3 are the efficiency parameters introduced to account for the scale-dependent behavior of CNTs. In the present study, Poisson's ratio $v(z)$ of the CNTs and the matrix constituents is expressed as follows:

$$v(z) = V_{CNTs}(z) v_{CNTs} + V_m(z) v_m \tag{4}$$

2.2 Basic Formulation

In this investigation, the first-order shear deformation theory is employed. The corresponding kinematic assumptions are introduced through the displacement field, which is expressed as:

$$\begin{cases} u(x, y, z, t) = u_0(x, y, t) - z\beta_x(x, y, t) \\ v(x, y, z, t) = v_0(x, y, t) - z\beta_y(x, y, t) \\ w(x, y, z, t) = w_0(x, y, t) \end{cases} \tag{5}$$

here, u_0 and v_0 represent the in-plane displacements, while w_0 denotes the transverse displacement at a point on the mid-plane of the CNTRC plate. The rotations of the normal to the mid-surface, due to transverse shear deformation, are represented by β_x and β_y about the y- and x-axes, respectively. The strain components associated with the displacement field defined in Eq. (5) are given as follows:

$$\begin{Bmatrix} \varepsilon_x \\ \varepsilon_y \\ \gamma_{xy} \end{Bmatrix} = \begin{Bmatrix} \varepsilon_x^m \\ \varepsilon_y^m \\ \gamma_{xy}^m \end{Bmatrix} + z \begin{Bmatrix} \chi_x \\ \chi_y \\ \chi_{xy} \end{Bmatrix} \tag{6}$$

$$\begin{Bmatrix} \gamma_{xz} \\ \gamma_{yz} \end{Bmatrix} = \begin{Bmatrix} \gamma_{xz}^s \\ \gamma_{yz}^s \end{Bmatrix}$$

where

$$\begin{Bmatrix} \varepsilon_x^m \\ \varepsilon_y^m \\ \gamma_{xy}^m \end{Bmatrix} = \begin{Bmatrix} u_{0,x} \\ v_{0,y} \\ u_{0,y} + v_{0,x} \end{Bmatrix}, \begin{Bmatrix} \chi_x \\ \chi_y \\ \chi_{xy} \end{Bmatrix} = - \begin{Bmatrix} \beta_{x,x} \\ \beta_{y,y} \\ \beta_{x,y} + \beta_{y,x} \end{Bmatrix}, \begin{Bmatrix} \gamma_{xz}^s \\ \gamma_{yz}^s \end{Bmatrix} = \begin{Bmatrix} w_{0,x} - \beta_x \\ v_{0,y} - \beta_y \end{Bmatrix} \tag{7}$$

The constitutive relations for the CNTRC plate are formulated based on the linear elasticity theory for orthotropic materials. These relations define the stress-strain behavior in terms of the effective material properties, which vary through the thickness according to the presented CNTs distribution patterns as:

$$\begin{Bmatrix} \sigma_x \\ \sigma_y \\ \tau_{xy} \\ \tau_{xz} \\ \tau_{yz} \end{Bmatrix} = \begin{bmatrix} Q_{11} & Q_{12} & 0 & 0 & 0 \\ Q_{12} & Q_{22} & 0 & 0 & 0 \\ 0 & 0 & Q_{66} & 0 & 0 \\ 0 & 0 & 0 & Q_{44} & 0 \\ 0 & 0 & 0 & 0 & Q_{55} \end{bmatrix} \begin{Bmatrix} \varepsilon_x \\ \varepsilon_y \\ \gamma_{xy} \\ \gamma_{xz} \\ \gamma_{yz} \end{Bmatrix} \tag{8}$$

The stiffness coefficients Q_{ij}, associated with the CNT reinforced nanocomposite material, are defined in terms of the effective elastic constants as follows:

$$Q_{11} = \frac{E_{11}(z)}{1 - v_{21}v_{12}};\ Q_{22} = \frac{E_{22}(z)}{1 - v_{21}v_{12}};\ Q_{12} = \frac{v_{21}E_{11}(z)}{1 - v_{21}v_{12}};\ Q_{66} = G_{12}(z);\ Q_{44} = k_s G_{13}(z);\ Q_{55} = k_s G_{23}(z) \tag{9}$$

here, k_s denotes the shear correction factor, which is taken as 5/6.

2.3 Variational Formulation

The governing equations of the CNTRC nanocomposite plate are derived using Hamilton's variational principle, which accounts for the balance of strain energy and kinetic energy as follows:

$$\int_{t_1}^{t_2} \delta\left(\Pi_P - \Pi_K\right) dt = 0 \tag{10}$$

In this expression, $\delta\Pi_P$ denotes the variation of the strain energy of the CNT reinforced nanocomposite plate, while $\delta\Pi_K$ represents the variation of kinetic energy. The strain energy variation is given by:

$$\begin{aligned} \delta\Pi_P &= \int_V \left(\sigma_x\delta\varepsilon_x + \sigma_y\delta\varepsilon_y + \tau_{xz}\delta\gamma_{xz} + \tau_{yz}\delta\gamma_{yz} + \tau_{xy}\delta\gamma_{xy}\right) dV \\ &= \int_{-a/2}^{+a/2}\int_{-b/2}^{+b/2} \left(N_x\delta\varepsilon_x^m + N_y\delta\varepsilon_y^m + N_{xy}\delta\gamma_{xy}^m + M_x\delta\chi_x + M_y\delta\chi_y + M_{xy}\delta\chi_{xy}\right. \\ &\quad \left. + S_{xz}\delta\gamma_{xz}^s + S_{yz}\delta\gamma_{yz}^s\right) dxdy \end{aligned} \tag{11}$$

The stress resultants, including the membrane forces N, bending moments M, and transverse shear forces S, are obtained by integrating the corresponding stress components through the thickness of the CNT reinforced nanocomposite plate:

$$\begin{Bmatrix} N_{ij} \\ M_{ij} \end{Bmatrix} = \int_{-h/2}^{+h/2} \sigma_{ij} \begin{Bmatrix} 1 \\ z \end{Bmatrix} dz;\ (ij = x, y, xy)\ and\ S_{ij} = \int_{-h/2}^{+h/2} \tau_{ij} dz;\ (j = xz, yz) \tag{12}$$

By substituting Eqs. (8) and (9) into Eq. (11), the final expressions for the stress resultants are obtained in the following form:

$$\begin{Bmatrix} N_{ij} \\ M_{ij} \\ S_{ij} \end{Bmatrix} = \begin{bmatrix} A_{ij} & B_{ij} & 0 \\ B_{ij} & D_{ij} & 0 \\ 0 & 0 & A_{Sij} \end{bmatrix} \begin{Bmatrix} \varepsilon_{ij}^{m} \\ \chi_{ij} \\ \gamma_{ij}^{s} \end{Bmatrix} \tag{13}$$

The detailed expressions for the stiffness coefficients are given as follows:

$$\left[A_{ij}\right] = \begin{bmatrix} A_{11} & A_{12} & 0 \\ A_{12} & A_{22} & 0 \\ 0 & 0 & A_{66} \end{bmatrix}; \left[B_{ij}\right] = \begin{bmatrix} B_{11} & B_{12} & 0 \\ B_{12} & B_{22} & 0 \\ 0 & 0 & B_{66} \end{bmatrix}; \left[D_{ij}\right] = \begin{bmatrix} D_{11} & D_{12} & 0 \\ D_{12} & D_{22} & 0 \\ 0 & 0 & D_{66} \end{bmatrix}; \left[A_{Sij}\right] = \begin{bmatrix} A_{s44} & 0 \\ 0 & A_{s55} \end{bmatrix} \tag{14}$$

where

$$\begin{Bmatrix} A_{ij} \\ B_{ij} \\ D_{ij} \end{Bmatrix} = \int_{-h/2}^{+h/2} Q_{ij} \begin{Bmatrix} 1 \\ z \\ z^2 \end{Bmatrix} dz \; (ij = 11, 12, 22, 66) \; and \; \begin{Bmatrix} A_{s44} \\ A_{s55} \end{Bmatrix} = k_s \int_{-h/2}^{+h/2} \begin{Bmatrix} Q_{44} \\ Q_{55} \end{Bmatrix} dz \tag{15}$$

The variation of kinetic energy for the CNT-reinforced nanocomposite plate is expressed as follows:

$$\begin{aligned} \delta\Pi_K &= \int_V \rho(z) \left(\dot{u}\delta\dot{u} + \dot{v}\delta\dot{v} + \dot{w}\delta\dot{w}\right) dV \\ &= \int_{-a/2}^{+a/2} \int_{-b/2}^{+b/2} \left[I_0\dot{u}_0\delta\dot{u}_0 + I_0\dot{v}_0\delta\dot{v}_0 + I_0\dot{w}_0\delta\dot{w}_0 - I_1\left(\dot{u}_0\delta\dot{\beta}_x + \dot{\beta}_x\delta\dot{u}_0\right)\right. \\ &\quad \left. - I_1\left(\dot{v}_0\delta\dot{\beta}_y + \dot{\beta}_y\delta\dot{v}_0\right) + I_2\left(\dot{\beta}_x\delta\dot{\beta}_x + \dot{\beta}_y\delta\dot{\beta}_y\right)\right] dxdy \end{aligned} \tag{16}$$

here, $\rho\,(z)$ denotes the mass density varying through the thickness, $(I_0, I_1$ and $I_2)$ represent the mass inertia terms, defined as follows:

$$\begin{Bmatrix} I_0 \\ I_1 \\ I_2 \end{Bmatrix} = \int_{-h/2}^{h/2} \rho\,(z) \begin{Bmatrix} 1 \\ z \\ z^2 \end{Bmatrix} dz \tag{17}$$

By substituting Eqs. (11) and (16) into Eq. (10), and expressing the $\delta\Pi_P$ and $\delta\Pi_K$ variations in explicit form, followed by the application of integration by parts and setting the virtual displacements δu_0, δv_0, δw_0, $\delta\beta_x$ and $\delta\beta_y$, the weak variational form of the governing equations for the CNT-reinforced plate is derived as follows:

$$\begin{aligned} &\int_{ds} \left(\langle\delta\varepsilon^m\rangle\left[A\right]\left\{\varepsilon^m\right\} + \langle\delta\varepsilon^m\rangle\left[B\right]\left\{\chi\right\} + \langle\delta\chi\rangle\left[B\right]\left\{\varepsilon^m\right\} + \langle\delta\chi\rangle\left[D\right]\left\{\chi\right\} + \langle\delta\gamma^s\rangle\left[A_s\right]\left\{\gamma^s\right\} + \langle\delta u_0\rangle I_0\left\{\ddot{u}_0\right\}\right. \\ &\quad + \langle\delta v_0\rangle I_0\left\{\ddot{v}_0\right\} + \langle\delta w_0\rangle I_0\left\{\ddot{w}_0\right\} - \langle\delta u_0\rangle I_1\left\{\ddot{\beta}_x\right\} - \langle\delta\beta_x\rangle I_1\left\{\ddot{u}_0\right\} - \langle\delta v_0\rangle I_1\left\{\ddot{\beta}_y\right\} - \left\langle\delta\beta_y\right\rangle I_1\left\{\ddot{v}_0\right\} + \langle\delta\beta_x\rangle I_2\left\{\ddot{\beta}_x\right\} \\ &\quad \left. + \left\langle\delta\beta_y\right\rangle I_2\left\{\ddot{\beta}_y\right\}\right) ds = 0 \end{aligned} \tag{18}$$

Consequently, the weak form presented in Eq. (18) can be discretized and reformulated into the standard matrix form of the governing equations:

$$\left(K_m + K_{mb} + K_{bm} + K_b + K_s\right)\{d_i\} + \left(M_{u_0} + M_{v_0} + M_{w_0} - M_{u_0\beta_x} - M_{\beta_x u_0} - M_{v_0\beta_y} - K_{\beta_y v_0} + M_{\beta_x} + M_{\beta_y}\right)\left\{\ddot{d}_i\right\} = 0 \tag{19}$$

2.4 New Improved IQ4 Finite Element Formulation

A new finite element model is proposed for FG-CNTRC plates based on the FSDT assumptions. The formulation enhances the classical Q4 membrane part by incorporating side-based average projection to accurately evaluate membrane–bending coupling, which is essential for graded composite materials. To avoid shear locking, the shear strain projection method is employed. This combination leads to an improved and advanced element formulation with enhanced accuracy and convergence performance.

2.4.1 IQ4 Finite Element Stiffness Matrix

The fundamental idea is to replace the normal strain components ε_x and ε_y by their averaged values over the element domain. Unlike the standard Q4 element, which ignores edge orientations, the proposed *B*-type method incorporates side-based projections for the element geometry. This modification effectively avoids locking under near-incompressible conditions and improves membrane strain accuracy, particularly for distorted or refined meshes. The position vector of any point *M* located on the mid-surface of the element can be interpolated from the nodal coordinates using the standard bilinear isoparametric shape functions, which depend explicitly on the natural coordinates ξ and η, as follows:

$$N_{i=1,2,3,4}\left(\xi_i, \eta_i\right) = \frac{1}{4}\left(1 + \xi_i\xi\right)\left(1 + \eta_i\eta\right)\xi_i \in [-1, +1] \text{ and } \eta_i \in [-1, +1] \tag{20}$$

The derivatives with respect to the physical coordinates (x, y) are obtained through the Jacobian matrix transformation.

$$\frac{\partial N_i}{\partial x} = J^{-1}\frac{\partial N_i}{\partial \xi}; \frac{\partial N_i}{\partial y} = J^{-1}\frac{\partial N_i}{\partial \eta} \tag{21}$$

where

$$J = \begin{bmatrix} \frac{\partial x}{\partial \xi} & \frac{\partial x}{\partial \eta} \\ \frac{\partial y}{\partial \xi} & \frac{\partial y}{\partial \eta} \end{bmatrix} = \sum_{i=1}^{4} \begin{Bmatrix} x_i \\ y_i \end{Bmatrix} \left\langle \frac{\partial N_i}{\partial \xi}; \frac{\partial N_i}{\partial \eta} \right\rangle \tag{22}$$

The average strains over the element are computed using numerical integration based on a 2 × 2 Gauss quadrature scheme.

$$\tilde{\varepsilon}_x = \frac{1}{4}\sum_{i=1}^{4} \varepsilon_x\left(\xi_i, \eta_i\right), \tilde{\varepsilon}_y = \frac{1}{4}\sum_{i=1}^{4} \varepsilon_y\left(\xi_i, \eta_i\right) \tag{23}$$

The modified matrix is explicitly expressed as follows:

$$\tilde{B}_m = \begin{Bmatrix} \tilde{B}_x \\ \tilde{B}_y \\ B_{xy} \end{Bmatrix} \tag{24}$$

where the modified components are explicitly defined as:

$$\tilde{B}_x = \frac{1}{4}\sum_{i=1}^{4} B_x^m\left(\xi_i,\eta_i\right), \tilde{B}_y = \frac{1}{4}\sum_{i=1}^{4} B_y^m\left(\xi_i,\eta_i\right) \tag{25}$$

with the initial components given by:

$$\begin{Bmatrix} B_x^m \\ B_y^m \\ B_{xy} \end{Bmatrix} = [J]^{-1}[\partial\xi]\begin{bmatrix} N_i & 0 & \\ 0 & N_i & \cdots \\ N_i & N_i & \end{bmatrix} and\ [\partial\xi] = \begin{bmatrix} (),_\xi & 0 \\ (),_\xi & 0 \\ 0 & (),_\eta \\ 0 & (),_\eta \end{bmatrix} \tag{26}$$

The final expression of the modified $\tilde{B}_m$ matrix corresponding to the membrane part is given by:

$$\tilde{B}_m = \begin{bmatrix} \frac{1}{4}\sum_{j=1}^{4}\left(J_{11}^{-1}N_{i,\xi}\big|_j + J_{12}^{-1}N_{i,\eta}\big|_j\right) & 0 & 0 & 0 & 0 & \\ 0 & \frac{1}{4}\sum_{j=1}^{4}\left(J_{21}^{-1}N_{i,\xi}\big|_j + J_{22}^{-1}N_{i,\eta}\big|_j\right) & 0 & 0 & 0 & \cdots \\ \left(J_{21}^{-1}N_{i,\xi} + J_{22}^{-1}N_{i,\eta}\right) & \left(J_{11}^{-1}N_{i,\xi} + J_{12}^{-1}N_{i,\eta}\right) & 0 & 0 & 0 & \end{bmatrix}_{i=1,2,3,4} \tag{27}$$

Finally, the membrane stiffness contribution is expressed as:

$$[K_m] = \int_{-1}^{+1}\int_{-1}^{+1}\left[\tilde{B}_m\right]^T\left[A_{ij}\right]\left[\tilde{B}_m\right]|J|\,\partial\xi\partial\eta \tag{28}$$

The variation of the strain energy associated with the bending deformation of the CNTRC plate is expressed as:

$$\delta K_b = \int_{ds}\langle\delta\chi\rangle\left[D_{ij}\right]\{\chi\}\,ds \tag{29}$$

with

$$\chi = \begin{Bmatrix} -\beta_{x,x} \\ -\beta_{y,y} \\ -\left(\beta_{x,y}+\beta_{y,x}\right) \end{Bmatrix} = [B_b]\begin{Bmatrix}\beta_x \\ \beta_y\end{Bmatrix} \tag{30}$$

The rotations of the normal to the mid-surface are interpolated using a bilinear shape function of the Q4 element, and are given by:

$$\begin{Bmatrix}\beta_x \\ \beta_y\end{Bmatrix} = \sum_{i=1}^{4}\langle N_i\rangle\begin{Bmatrix}\beta_{xi} \\ \beta_{yi}\end{Bmatrix} \tag{31}$$

where the differential operator matrix $[B_b]$ associated with the bending stiffness part is defined as:

$$[B_b] = \begin{bmatrix} 0 & 0 & 0 & \left(J_{11}^{-1}N_{i,\xi} + J_{12}^{-1}N_{i,\eta}\right) & 0 & \cdots \\ 0 & 0 & 0 & 0 & \left(J_{21}^{-1}N_{i,\xi} + J_{22}^{-1}N_{i,\eta}\right) & \cdots \\ 0 & 0 & 0 & \left(J_{21}^{-1}N_{i,\xi} + J_{22}^{-1}N_{i,\eta}\right) & \left(J_{11}^{-1}N_{i,\xi} + J_{12}^{-1}N_{i,\eta}\right) & \cdots \end{bmatrix}_{i=1,2,3,4} \tag{32}$$

Finally, the bending stiffness contribution is expressed as:

$$[K_b] = \int_{-1}^{+1}\int_{-1}^{+1} [B_b]^T [D_{ij}] [B_b] |J| \, \partial\xi\partial\eta \tag{33}$$

In the present formulation, membrane–bending coupling is evaluated through an enhanced membrane strain–displacement matrix $\tilde{B}_m$, specifically developed to reflect the interaction neglected in classical models. This coupling is important for accurately representing asymmetric through-thickness CNT distribution patterns:

$$[K_{mb}] = [K_{bm}] = \int_{-1}^{+1}\int_{-1}^{+1} [\tilde{B}_m]^T [B_{ij}] [B_b] |J| \, \partial\xi\partial\eta \tag{34}$$

This study adopts the discrete shear projection technique to avoid shear locking without introducing spurious modes or sensitivity to mesh distortion [42–45]. Refining the shear strain field within the Q4γ element achieves accurate shear deformation across various thicknesses without additional variables or reduced integration. The resulting formulation remains efficient and stable for both thick and thin plates. The variation of the shear strain energy is given by:

$$\delta K_s = \int_{ds} \langle \delta\gamma^s \rangle [A_s] \{\gamma^s\} \, ds \tag{35}$$

with

$$\begin{Bmatrix} \gamma^s_{xz} \\ \gamma^s_{yz} \end{Bmatrix} = \begin{Bmatrix} w_{0,x} - \beta_x \\ w_{0,y} - \beta_y \end{Bmatrix} \tag{36}$$

and in isosparametric coordinates:

$$\begin{Bmatrix} \gamma^s_{\xi z} \\ \gamma^s_{\eta z} \end{Bmatrix} = \begin{Bmatrix} w_{0,\xi} - \beta_\xi \\ w_{0,\eta} - \beta_\eta \end{Bmatrix} = [B_\xi] \{d_e\} \tag{37}$$

In matrix form:

$$[B_\xi] = \begin{bmatrix} 0 & 0 & N_{i,\xi} & \xi_i N_{i,\xi} & 0 & \cdots \\ 0 & 0 & N_{i,\eta} & 0 & \eta_i N_{i,\eta} & \cdots \end{bmatrix}_{i=1,2,3,4} \tag{38}$$

Eq. (37) defines the transverse shear deformation along each side of the plate element in terms of the nodal displacement parameters:

$$\int_{-1}^{1} \left[\gamma_{\xi z} - \left(\frac{\partial w_0}{\partial \xi} - \varphi_\xi \right) \right] d\xi = 0$$

$$\int_{-1}^{1} \left[\gamma_{\eta z} - \left(\frac{\partial w_0}{\partial \eta} - \varphi_\eta \right) \right] d\eta = 0 \tag{39}$$

The transverse shear strain components γ are then interpolated over the element using the projected side values as:

$$\gamma = \sum_{i=1}^{4} N_i^{\gamma}(\xi,\eta)\,\gamma_{jk} \tag{40}$$

where N_i^{γ} are the interpolation functions associated with the element sides, and γ_{jk} are the corresponding constant shear strains projected along each side. The transverse shear strain field is interpolated from side-based constant values using appropriate shape functions as:

$$\begin{cases} \gamma_{\xi}^{ij} = \dfrac{1}{2}(1-\eta)\,\gamma_{\xi}^{12} + \dfrac{1}{2}(1+\eta)\,\gamma_{\xi}^{34} \\ \gamma_{\eta}^{ij} = \dfrac{1}{2}(1-\xi)\,\gamma_{\xi}^{13} + \dfrac{1}{2}(1+\xi)\,\gamma_{\xi}^{24} \end{cases} \tag{41}$$

The B_{ξ} matrix corresponding to the shear strain–displacement relation is defined as:

$$\left[B_{\xi}\right] = \begin{bmatrix} 0 & 0 & N_{i,\xi} & \xi_i N_{i,\xi} J_{11}^{-1} & \xi_i N_{i,\xi} J_{12}^{-1} & \cdots \\ 0 & 0 & N_{i,\eta} & \eta_i N_{i,\eta} J_{21}^{-1} & \eta_i N_{i,\eta} J_{22}^{-1} & \cdots \end{bmatrix}_{i=1,2,3,4} \tag{42}$$

and

$$\left[B_s\right] = [J]^{-1}\left[B_{\xi}\right] \tag{43}$$

The shear stiffness contribution is expressed as:

$$\left[K_s\right] = \int_{-1}^{+1}\int_{-1}^{+1} \left[B_s\right]^T \left[\left[A_s\right]\right]\left[B_s\right]|J|\,\partial\xi\partial\eta \tag{44}$$

Finally, the element stiffness matrix for the IQ4 element, which includes membrane, bending, membrane–bending coupling, and transverse shear effects, is expressed as:

$$\left[K^e\right] = \left[K_m\right] + \left[K_{mb}\right] + \left[K_{bm}\right] + \left[K_b\right] + \left[K_s\right] \tag{45}$$

2.4.2 IQ4 Finite Element Mass Matrix

The IQ4 mass matrix is derived from the virtual variation of kinetic energy. This formulation considers translational and rotational inertial effects, including the coupling terms arising from asymmetric mass distribution through the plate thickness. Based on the weak form of the kinetic energy of the CNT-reinforced nanocomposite plate, the mass matrix may be expressed by:

$$\begin{aligned} \delta\Pi_K = \int_{ds} \big(I_0 \big(\langle\ \ \delta u_0\rangle \{\ddot{u}_0\} + \langle\delta v_0\rangle \{\ddot{v}_0\} + \langle\delta w_0\rangle \{\ddot{w}_0\}\big) \\ - I_1\big(\langle\delta u_0\rangle\{\ddot{\beta}_x\} + \langle\delta\beta_x\rangle\{\ddot{u}_0\}\langle\delta v_0\rangle I_1\{\ddot{\beta}_y\} + \langle\delta\beta_y\rangle I_1\{\ddot{v}_0\}\big) \\ + I_2\big(\langle\delta\beta_x\rangle\{\ddot{\beta}_x\} + \langle\delta\beta_y\rangle\{\ddot{\beta}_y\}\big)\big)\,ds \end{aligned} \tag{46}$$

The bilinear isoparametric shape functions $N_i(\xi, \eta)$ are employed to interpolate the translational and rotational degrees of freedom within the element domain:

$$\{d_T\} = \begin{bmatrix} N_i & 0 & 0 \\ 0 & N_i & 0 \\ 0 & 0 & N_i \end{bmatrix} \begin{Bmatrix} u_0 \\ v_0 \\ w_0 \end{Bmatrix}_{i=1,2,3,4} \tag{47}$$

and,

$$\{d_R\} = \begin{bmatrix} N_i & 0 \\ 0 & N_i \end{bmatrix} \begin{Bmatrix} \beta_x \\ \beta_y \end{Bmatrix}_{i=1,2,3,4} \tag{48}$$

where $\{d_T\}$ and $\{d_R\}$ are the translational and rotational d.o.f, respectively. Accordingly, the final expression of the computed element mass matrix is given by:

$$[M^e] = \int_{ds} \left(N_T^T I_0 N_T^T - N_T^T I_1 N_R^T - N_R^T I_1 N_T^T + N_R^T I_2 N_R^T \right) ds \tag{49}$$

where

$$[M^e] = \begin{bmatrix} M_T & M_{RT} \\ M_{RT} & M_R \end{bmatrix} \tag{50}$$

By assembling the contributions from all elements, the global stiffness matrix K_g and the global mass matrix M_g are obtained as:

$$[K]_g = \sum_{e=1}^{n} [K^e] \; and \; [M]_g = \sum_{e=1}^{n} [M^e] \tag{51}$$

After rewriting Eq. (19), the free vibration eigenvalue analysis is obtained in the form:

$$\left([K]_g - \omega^2 [M]_g \right) \{d\} = 0 \tag{52}$$

In Eq. (52), ω denotes the system's natural frequencies. All element matrices are integrated using a 2 × 2 Gauss quadrature scheme, ensuring sufficient numerical accuracy for evaluating stiffness and mass contributions.

3 Numerical Simulation and Discussion

This section provides a series of computational examples to assess the accuracy and robustness of the formulated IQ4 model in predicting the free vibration behavior of FG-CNTRC nanocomposite plates. Both comparative and parametric studies are carried out, drawing on reference solutions available in the literature for validation purposes. The FG-CNTRC plates analyzed in this study feature various CNT distributions embedded within a polymer matrix. Detailed information on the material properties and volume fractions is presented in Tables 1–3. The boundary conditions applied in each case are summarized in Table 4. A systematic investigation evaluates the effects of CNT distribution patterns, material gradation, and geometric parameters, including central cutouts. Both intact plates and those with cutouts are examined, allowing for

a clear assessment of the cutout size and shape influence the dynamic response. To ensure consistency and facilitate comparison, the natural frequencies are reported in normalized form [14,31]:

$$\overline{\omega} = \omega\left(\frac{a^2}{h}\right)\sqrt{\frac{\rho_m}{D_m}};\ D_m = \frac{E_m h^2}{12\left(1-\nu_m^2\right)} \tag{53}$$

Table 1: Mechanical properties of the matrix and the CNTs reinforcement [14,31]

Component	Young modulus E (GPa)	Mass density ρ (kg/m^3)	Poisson's ratio ν
Epoxy/Polymer matrix	2.5	1150	0.34
CNTs	E_{11} = 5646.6; E_{22} = 7080	1400	0.175

Table 2: CNTs efficiency parameters [14,31]

V_{CNT}	η_1	η_2	η_3
0.17	0.142	1.626	0.7 η_2

Table 3: The calculated final material properties of FG-UD nanocomposite plates (V_{CNT} = 0.17)

E_{11} (GPa)	E_{22} (GPa)	G_{12} (GPa)	G_{13} (GPa)	G_{23} (GPa)	ν_{12}	ν_{21}	ρ (kg/m^3)
138.3839	4.8972	1.2791	1.2791	1.2791	0.3120	0.0110	1192.5

Table 4: Boundary conditions were used in the present study

BCs	$x = -a/2, a/2$	$y = -b/2, b/2$
SSSS	$u_0 = w_0 = \beta_y = 0$	$v_0 = w_0 = \beta_x = 0$
CCCC	$u_0 = v_0 = w_0 = \beta_x = \beta_y = 0$	$u_0 = v_0 = w_0 = \beta_x = \beta_y = 0$
CFCF	$u_0 = v_0 = w_0 = \beta_x = \beta_y = 0$	$u_0 \neq v_0 \neq w_0 \neq \beta_x \neq \beta_y \neq 0$

The first example provides a convergence study to assess the performance of the proposed IQ4 finite element in the free vibration analysis of CNT-reinforced plates. Fig. 3 presents results for FG-UD and FG-X distribution patterns, respectively, with comparisons made against the classical Q4 element using selective reduced integration. Across both patterns, the IQ4 element demonstrates faster and more stable convergence, achieving accurate fundamental frequencies with fewer mesh divisions. In contrast, the Q4 element shows slower convergence and higher sensitivity to mesh refinement. These results confirm the improved numerical robustness and efficiency of the IQ4 formulation, making it particularly suitable for analyzing nanocomposite plates with advanced material gradations. The next section investigates the vibrational behavior of FG-CNTRC plates with central cutouts through a comparative analysis against benchmark solutions reported by Mirzaei and Kiani [31] and Mirzaei [14]. The IQ4 finite element model demonstrates excellent agreement with the reference Ritz-based results across various CNT distribution configurations. For clarity, the results are presented separately: Tables 5–8 correspond to simply supported plates, whereas Tables 9–12 report the case of fully clamped plates. Notably, the IQ4 element effectively captures both in-plane and transverse shear effects induced by material gradation, while maintaining reduced computational cost compared to the high-order Ritz and Ritz–Chebyshev approaches. As consistently observed, the FG-X distribution exhibits the

highest natural frequencies due to the concentration of CNTs near the plate surfaces, thereby enhancing bending stiffness.

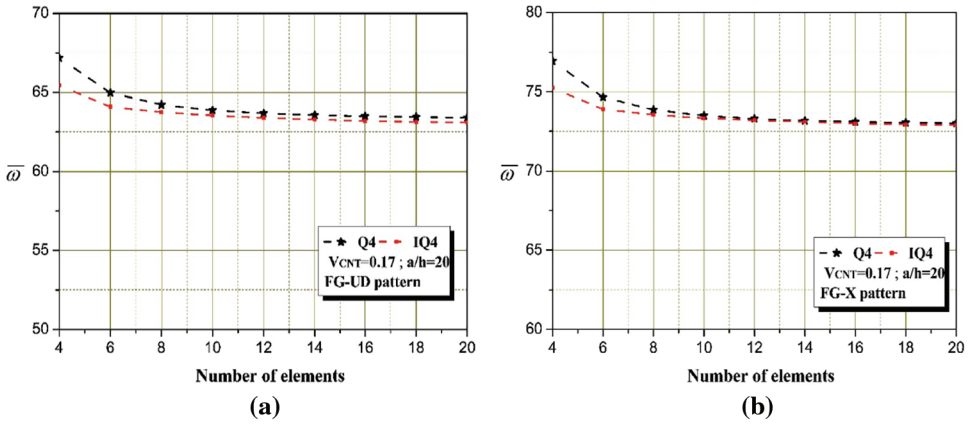

Figure 3: Convergence comparison of fundamental frequency using classical Q4 and improved IQ4 elements for CNT-reinforced plates with different CNTs distribution patterns: (**a**) FG-UD pattern; (**b**) FG-X

Table 5: Investigation of the first four dimensionless frequencies of FG-UD CNTRC nanocomposite simply-supported plates with central cutouts (a/b = 1, a/h = 20, V_{CNT} = 0.17 and various cutout aspect ratios)

c/a	Models	$\overline{\omega}_1$	$\overline{\omega}_2$	$\overline{\omega}_3$	$\overline{\omega}_4$
0	Ritz-FSDT [31]	63.2598	83.2741	132.0746	143.7036
	Present	63.2957	83.2834	132.0494	140.6680
0.1	Ritz-FSDT [31]	62.8020	83.1849	131.8828	144.8261
	Present	61.1788	83.0629	131.4948	145.7748
0.3	Ritz-FSDT [31]	52.8233	78.3506	111.6736	130.6302
	Present	51.7910	77.5376	107.3200	129.2882
0.5	Ritz-FSDT [31]	49.7695	72.2115	75.6430	110.4459
	Present	49.0996	71.6079	73.2652	107.1577

Table 6: Investigation of the first four dimensionless frequencies of FG-V CNTRC nanocomposite simply-supported plates with central cutouts (a/b = 1, a/h = 20, V_{CNT} = 0.17 and various cutout aspect ratios)

c/a	Models	$\overline{\omega}_1$	$\overline{\omega}_2$	$\overline{\omega}_3$	$\overline{\omega}_4$
0	Ritz-FSDT [31]	55.2524	78.2905	130.3768	144.7268
	Present	55.3600	78.4845	130.4763	141.9702
0.1	Ritz-FSDT [31]	54.8235	78.1925	130.2147	145.8510
	Present	62.4889	85.2564	129.0723	146.7707
0.3	Ritz-FSDT [31]	46.7420	73.0816	107.2829	129.9159
	Present	62.7300	65.1645	104.4452	127.5728
0.5	Ritz-FSDT [31]	45.0900	66.7584	73.9966	108.6995
	Present	42.0709	65.8099	74.6212	102.4068

Table 7: Investigation of the first four dimensionless frequencies of FG-O CNTRC nanocomposite simply-supported plates with central cutouts (a/b = 1, a/h = 20, V_{CNT} = 0.17 and various cutout aspect ratios)

c/a	Models	$\overline{\omega}_1$	$\overline{\omega}_2$	$\overline{\omega}_3$	$\overline{\omega}_4$
0	Ritz-FSDT [31]	49.4292	49.4292	123.2571	144.7344
	Present	49.4678	49.4678	123.2670	142.0210
0.1	Ritz-FSDT [31]	49.0286	72.4102	123.0916	145.8609
	Present	47.1810	72.2726	121.2397	145.7748
0.3	Ritz-FSDT [31]	41.9863	67.4468	100.7698	123.2779
	Present	41.3124	66.6416	100.0194	122.0297
0.5	Ritz-FSDT [31]	40.9160	31.2728	69.6564	103.1278
	Present	40.5261	60.6878	67.3708	100.8114

Table 8: Investigation of the first four dimensionless frequencies of FG-X CNTRC nanocomposite simply-supported plates with central cutouts (a/b = 1, a/h = 20, V_{CNT} = 0.17 and various cutout aspect ratios)

c/a	Models	$\overline{\omega}_1$	$\overline{\omega}_2$	$\overline{\omega}_3$	$\overline{\omega}_4$
0	Ritz-FSDT [31]	72.8708	92.2430	141.7590	144.7344
	Present	72.8965	92.2035	141.5502	142.0210
0.1	Ritz-FSDT [31]	72.4414	92.1454	141.5884	145.8609
	Present	70.0160	92.0114	139.7606	145.7747
0.3	Ritz-FSDT [31]	60.5716	87.1986	119.1929	139.3437
	Present	59.8852	86.2815	114.7052	137.7016
0.5	Ritz-FSDT [31]	56.2066	80.5715	80.8909	118.0424
	Present	55.2970	80.1869	83.8524	116.2512

Table 9: Investigation of the first four dimensionless frequencies of FG-UD CNTRC nanocomposite fully clamped plates with central cutouts (a/b = 1, a/h = 20, V_{CNT} = 0.17 and various cutout aspect ratios)

c/a	Models	$\overline{\omega}_1$	$\overline{\omega}_2$	$\overline{\omega}_3$	$\overline{\omega}_4$
0	Ritz-FSDT [31]	104.7581	127.4624	177.3348	216.4439
	Ritz-Chebyshev FSDT [14]	104.7871	127.8264	178.7971	216.4614
	Present	104.8555	127.7297	178.3468	216.8847
0.1	Ritz-FSDT [31]	105.4667	127.4527	178.2958	210.3946
	Ritz-Chebyshev FSDT [14]	105.7780	127.7721	178.7566	210.8695
	Present	104.5621	127.4042	176.9683	210.2584

(Continued)

Table 9 (continued)

c/a	Models	$\overline{\omega}_1$	$\overline{\omega}_2$	$\overline{\omega}_3$	$\overline{\omega}_4$
0.3	Ritz-FSDT [31]	120.4439	126.9656	169.8070	188.2571
	Ritz-Chebyshev FSDT [14]	120.8667	127.2531	170.0702	188.8003
	Present	120.4666	126.0794	168.1927	187.1374
0.5	Ritz-FSDT [31]	144.3419	145.0951	220.7844	229.0503
	Ritz-Chebyshev FSDT [14]	145.5115	146.4002	222.2984	230.8655
	Present	143.8815	146.8993	222.2869	230.1312

Table 10: Investigation of the first four dimensionless frequencies of FG-V CNTRC nanocomposite fully clamped plates with central cutouts (a/b = 1, a/h = 20, V_{CNT} = 0.17 and various cutout aspect ratios)

c/a	Models	$\overline{\omega}_1$	$\overline{\omega}_2$	$\overline{\omega}_3$	$\overline{\omega}_4$
0	Ritz-FSDT [31]	97.1637	122.2427	175.0384	205.6517
	Ritz-Chebyshev FSDT [14]	97.2016	122.6404	176.5811	205.6906
	Present	97.2544	122.516	176.0846	206.1775
0.1	Ritz-FSDT [31]	97.5556	122.2235	175.8912	200.6315
	Ritz-Chebyshev FSDT [14]	97.8739	122.5515	176.3491	201.1100
	Present	93.5732	122.4598	176.7310	202.5817
0.3	Ritz-FSDT [31]	111.1976	120.2882	160.6058	183.8592
	Ritz-Chebyshev FSDT [14]	111.6316	120.5688	160.8451	184.3800
	Present	104.9553	116.8825	160.6379	181.0257
0.5	Ritz-FSDT [31]	137.8894	138.7569	208.3156	208.3156
	Ritz-Chebyshev FSDT [14]	138.4666	139.4295	209.8142	219.0137
	Present	137.1283	138.5251	205.7145	219.3500

Table 11: Investigation of the first four dimensionless frequencies of FG-O CNTRC nanocomposite fully clamped plates with central cutouts (a/b = 1, a/h = 20, V_{CNT} = 0.17 and various cutout aspect ratios)

c/a	Models	$\overline{\omega}_1$	$\overline{\omega}_2$	$\overline{\omega}_3$	$\overline{\omega}_4$
0	Ritz-FSDT [31]	90.1519	114.9774	166.5357	195.1187
	Ritz-Chebyshev FSDT [14]	90.1964	115.3363	167.9144	195.1793
	Present	90.2704	115.2563	167.5656	195.6660
0.1	Ritz-FSDT [31]	90.3317	114.9383	167.1189	190.7122
	Ritz-Chebyshev FSDT [14]	90.6542	115.2476	167.5834	191.1995
	Present	90.8394	114.8662	165.9004	189.9235

(Continued)

Table 11 (continued)

c/a	Models	$\overline{\omega}_1$	$\overline{\omega}_2$	$\overline{\omega}_3$	$\overline{\omega}_4$
0.3	Ritz-FSDT [31]	102.7080	112.4737	150.9616	174.3439
	Ritz-Chebyshev FSDT [14]	103.1452	112.7492	151.1918	174.8699
	Present	102.8673	111.5584	149.2400	172.7853
0.5	Ritz-FSDT [31]	129.1618	129.9906	196.1895	205.0887
	Ritz-Chebyshev FSDT [14]	129.7544	130.6752	197.6935	206.7070
	Present	127.8304	128.4866	197.5835	205.6650

Table 12: Investigation of the first four dimensionless frequencies of FG-X CNTRC nanocomposite fully clamped plates with central cutouts (a/b = 1, a/h = 20, V_{CNT} = 0.17 and various cutout aspect ratios)

c/a	Models	$\overline{\omega}_1$	$\overline{\omega}_2$	$\overline{\omega}_3$	$\overline{\omega}_4$
0	Ritz-FSDT [31]	112.9857	136.1313	187.5684	228.1375
	Ritz-Chebyshev FSDT [14]	113.0013	136.4831	189.0796	228.1233
	Present	113.0595	136.3417	188.4628	228.5125
0.1	Ritz-FSDT [31]	114.0739	136.1672	188.9056	221.1219
	Ritz-Chebyshev FSDT [14]	114.3648	136.4345	189.2184	221.6162
	Present	114.8811	136.0238	189.9235	218.4614
0.3	Ritz-FSDT [31]	130.6054	136.3973	181.1849	199.9691
	Ritz-Chebyshev FSDT [14]	131.0019	136.6431	181.4328	200.3748
	Present	130.5104	135.3890	181.9925	200.0749
0.5	Ritz-FSDT [31]	155.3892	156.2246	233.7825	242.7781
	Ritz-Chebyshev FSDT [14]	155.8463	156.7755	235.2230	244.1759
	Present	154.4608	157.6292	235.2517	243.4912

Conversely, with CNTs concentrated near the mid-plane, the FG-O pattern results in the lowest stiffness and frequencies. The FG-UD and FG-V distributions yield intermediate values, with FG-UD demonstrating higher stiffness attributed to its uniform reinforcement profile. This uniformity ensures that the reinforcing CNTs contribute consistently across the entire thickness, enhancing the stiffness. By contrast, while still effective, the FG-V distribution concentrates CNTs toward the surfaces, improving bending resistance locally but not providing the same balanced contribution throughout the plate. As a result, FG-UD exhibits slightly higher natural frequencies than FG-V, since its uniform stiffness distribution increases the global structural resistance to deformation. In contrast, FG-V shows a more mode-dependent sensitivity to bending and shear interactions. These trends are in close accordance with the reference data presented in Mirzaei and Kiani [31] and Mirzaei [14]. For plates with clamped–free (CFCF) boundary conditions on both sides, as presented in Tables 13–16, the proposed IQ4 model yields results that are in close agreement with the reference solutions. The frequency ordering FG-X > FG-UD > FG-V > FG-O is consistently maintained. Minor discrepancies are attributed to shear deformation treatments in thick plate configurations. Nonetheless, the IQ4 model achieves comparable accuracy with significantly reduced computational effort, confirming its suitability for large-scale parametric studies and practical engineering applications.

Table 13: Investigation of the first four dimensionless frequencies of FG-UD CNTRC nanocomposite CFCF plates with central cutouts (a/b = 1, a/h = 20, V_{CNT} = 0.17 and various cutout aspect ratios)

c/a	Models	$\overline{\omega}_1$	$\overline{\omega}_2$	$\overline{\omega}_3$	$\overline{\omega}_4$
0	Ritz-FSDT [31]	100.1209	100.5478	106.0262	130.1245
	Ritz-Chebyshev FSDT [14]	100.1628	100.5884	106.0609	130.1657
	Present	100.2584	100.6852	106.1573	130.2469
0.1	Ritz-FSDT [31]	100.2534	100.3429	106.3842	129.9112
	Ritz-Chebyshev FSDT [14]	100.5187	100.5980	106.5982	130.0777
	Present	100.1908	100.6904	105.6487	129.8107
0.3	Ritz-FSDT [31]	100.7600	101.2200	118.8467	128.0103
	Ritz-Chebyshev FSDT [14]	101.0124	101.4658	119.1584	127.0111
	Present	101.0968	101.5450	118.6661	128.3575
0.5	Ritz-FSDT [31]	101.6312	101.6706	134.2600	134.9668
	Ritz-Chebyshev FSDT [14]	101.8795	101.9136	134.0388	134.9972
	Present	101.9542	101.9876	131.2662	131.8858

Table 14: Investigation of the first four dimensionless frequencies of FG-V CNTRC nanocomposite CFCF plates with central cutouts (a/b = 1, a/h = 20, V_{CNT} = 0.17 and various cutout aspect ratios)

c/a	Models	$\overline{\omega}_1$	$\overline{\omega}_2$	$\overline{\omega}_3$	$\overline{\omega}_4$
0	Ritz-FSDT [31]	91.7731	92.3623	98.8950	125.5211
	Ritz-Chebyshev FSDT [14]	91.8200	92.4033	98.9357	125.5620
	Present	91.9235	92.5147	99.0610	125.6767
0.1	Ritz-FSDT [31]	91.8120	92.1557	99.0190	125.2861
	Ritz-Chebyshev FSDT [14]	92.0841	92.4114	99.2196	125.4391
	Present	83.6365	103.7556	117.7636	124.4332
0.3	Ritz-FSDT [31]	92.5250	93.0347	109.7041	121.8601
	Ritz-Chebyshev FSDT [14]	92.7802	93.2878	110.0218	120.6987
	Present	75.46126	89.8137	101.9569	115.4847
0.5	Ritz-FSDT [31]	93.5251	93.5551	126.8153	127.6207
	Ritz-Chebyshev FSDT [14]	93.7767	93.7994	126.6408	127.6781
	Present	67.1080	68.8748	124.8944	131.6732

Table 15: Investigation of the first four dimensionless frequencies of FG-O CNTRC nanocomposite CFCF plates with central cutouts (a/b = 1, a/h = 20, V_{CNT} = 0.17 and various cutout aspect ratios)

c/a	Models	$\overline{\omega}_1$	$\overline{\omega}_2$	$\overline{\omega}_3$	$\overline{\omega}_4$
0	Ritz-FSDT [31]	84.7084	85.3698	92.0274	118.2125
	Ritz-Chebyshev FSDT [14]	84.7650	85.4349	92.1063	118.3220
	Present	84.8710	85.5426	92.2125	118.4198

(Continued)

Table 15 (continued)

c/a	Models	$\overline{\omega}_1$	$\overline{\omega}_2$	$\overline{\omega}_3$	$\overline{\omega}_4$
0.1	Ritz-FSDT [31]	84.6851	85.1671	92.0179	117.9871
	Ritz-Chebyshev FSDT [14]	84.9619	85.4417	92.2475	118.2025
	Present	84.6394	85.5449	91.3555	117.9134
0.3	Ritz-FSDT [31]	85.4922	85.9562	101.4103	114.2352
	Ritz-Chebyshev FSDT [14]	85.7645	86.2236	101.7796	113.0819
	Present	85.8604	86.3160	101.4315	114.2222
0.5	Ritz-FSDT [31]	86.8830	86.5131	118.6095	119.3833
	Ritz-Chebyshev FSDT [14]	86.7629	86.7813	118.6271	119.6144
	Present	86.8426	86.8620	116.1825	116.8734

Table 16: Investigation of the first four dimensionless frequencies of FG-X CNTRC nanocomposite CFCF plates with central cutouts (a/b = 1, a/h = 20, V_{CNT} = 0.17 and various cutout aspect ratios)

c/a	Models	$\overline{\omega}_1$	$\overline{\omega}_2$	$\overline{\omega}_3$	$\overline{\omega}_4$
0	Ritz-FSDT [31]	108.3648	108.7314	114.1163	138.8282
	Ritz-Chebyshev FSDT [14]	108.4022	108.7544	114.0909	138.7229
	Present	108.4893	108.8425	114.1785	138.7812
0.1	Ritz-FSDT [31]	108.5295	108.6060	114.7279	138.6133
	Ritz-Chebyshev FSDT [14]	108.7655	108.8620	114.8865	138.6355
	Present	108.5687	108.8494	113.9385	138.3445
0.3	Ritz-FSDT [31]	108.9985	109.4736	128.8350	137.2623
	Ritz-Chebyshev FSDT [14]	109.2298	109.6954	129.0626	136.1666
	Present	109.3050	109.7638	128.4675	137.9427
0.5	Ritz-FSDT [31]	109.8563	109.9006	144.0598	144.7920
	Ritz-Chebyshev FSDT [14]	110.0719	110.1112	143.5786	144.5836
	Present	110.1370	110.1750	140.5959	141.2446

The influence of cutout geometry on the dynamic response is examined with particular attention to aspect ratio variations. As the longitudinal cutout ratio c/a increases, a marked reduction in effective stiffness is observed, particularly for the FG-O and FG-V distributions. This results in a corresponding decrease in natural frequencies. The sensitivity of the third mode to asymmetrical CNT gradation is also notable, indicating the role of in-plane stiffness in higher-order dynamic behavior. Further analysis of the effect of cutout dimensions is presented in Table 17, where variations in c/a and d/b are considered independently. It is observed that increases in c/a lead to a more significant frequency reduction than equivalent variations in d/b, for all CNT distribution patterns. This highlights the dominant influence of longitudinal stiffness reduction, particularly in distributions where axial reinforcement is less effective. The trend remains consistent across all FG configurations, reaffirming the enhanced stiffness contribution of outer-surface reinforcement (FG-X) and the reduced rigidity of mid-plane-oriented distributions (FG-O).

Table 17: Benchmark analysis of the first dimensionless frequency of simply supported CNTRC plates with various central cutout geometries and CNT distribution patterns (a/b = 1, a/h = 20, and V_{CNT} = 0.17)

c/a	d/c	FG-UD	FG-V	FG-O	FG-X
0	0.25	49.97959	48.496216	46.27385	54.27748
	0.5	49.97959	48.496216	46.27385	54.27748
	1	49.97959	48.496216	46.27385	54.27748
	2	49.97959	48.496216	46.27385	54.27748
0.1	0.25	48.90223	47.810552	45.69251	53.73502
	0.5	48.90223	47.810552	45.69251	53.73502
	1	47.49447	47.750200	45.41971	52.37798
	2	46.01692	45.933801	44.32308	50.93853
0.3	0.25	46.21696	44.801387	41.21541	47.87748
	0.5	45.99041	43.600615	40.30508	46.20286
	1	45.01434	42.457887	38.71061	45.41971
	2	44.88294	40.923911	37.91109	44.88294
0.5	0.25	44.33043	38.097021	36.98639	44.33043
	0.5	44.22016	38.660646	31.88088	44.22016
	1	41.79417	32.900894	29.89431	41.92621
	2	32.61140	28.789438	25.79424	34.81017

Fig. 4 illustrates the mesh and geometric configuration of square FG-CNTRC plates with central cutouts for varying cutout aspect ratios c/a, ranging from 0 (no cutout) to 0.5. As the cutout size increases, the effective cross-sectional area is reduced, thereby decreasing the global stiffness of the plate. This geometric simplification is crucial for systematically investigating the influence of cutout geometry on vibrational characteristics under simply supported boundary conditions. The mesh remains consistent across configurations to ensure convergence and maintain numerical stability in the frequency evaluation. Fig. 5 presents the variation of the first dimensionless natural frequencies as a function of both longitudinal (c/a) and transversal (d/b) cutout aspect ratios for four distinct CNT distribution patterns: FG-UD, FG-O, FG-X, and FG-A. Across all configurations, a progressive decrease in natural frequencies is observed as the cutout ratio increases, confirming that removing material significantly lowers the plate's bending stiffness. However, the longitudinal aspect ratio (c/a) effect is consistently more pronounced than the transversal one (d/b). This trend is particularly evident for FG-O and FG-V patterns, where reinforcement is concentrated near the mid-plane or distributed asymmetrically, reducing their effectiveness in resisting in-plane and flexural deformation. The FG-X configuration demonstrates the highest frequency values throughout the parametric range, which is attributable to the CNT reinforcement being concentrated near the plate surfaces, substantially enhancing the flexural rigidity. In contrast, FG-O consistently exhibits the lowest frequencies, as its central reinforcement minimizes bending resistance.

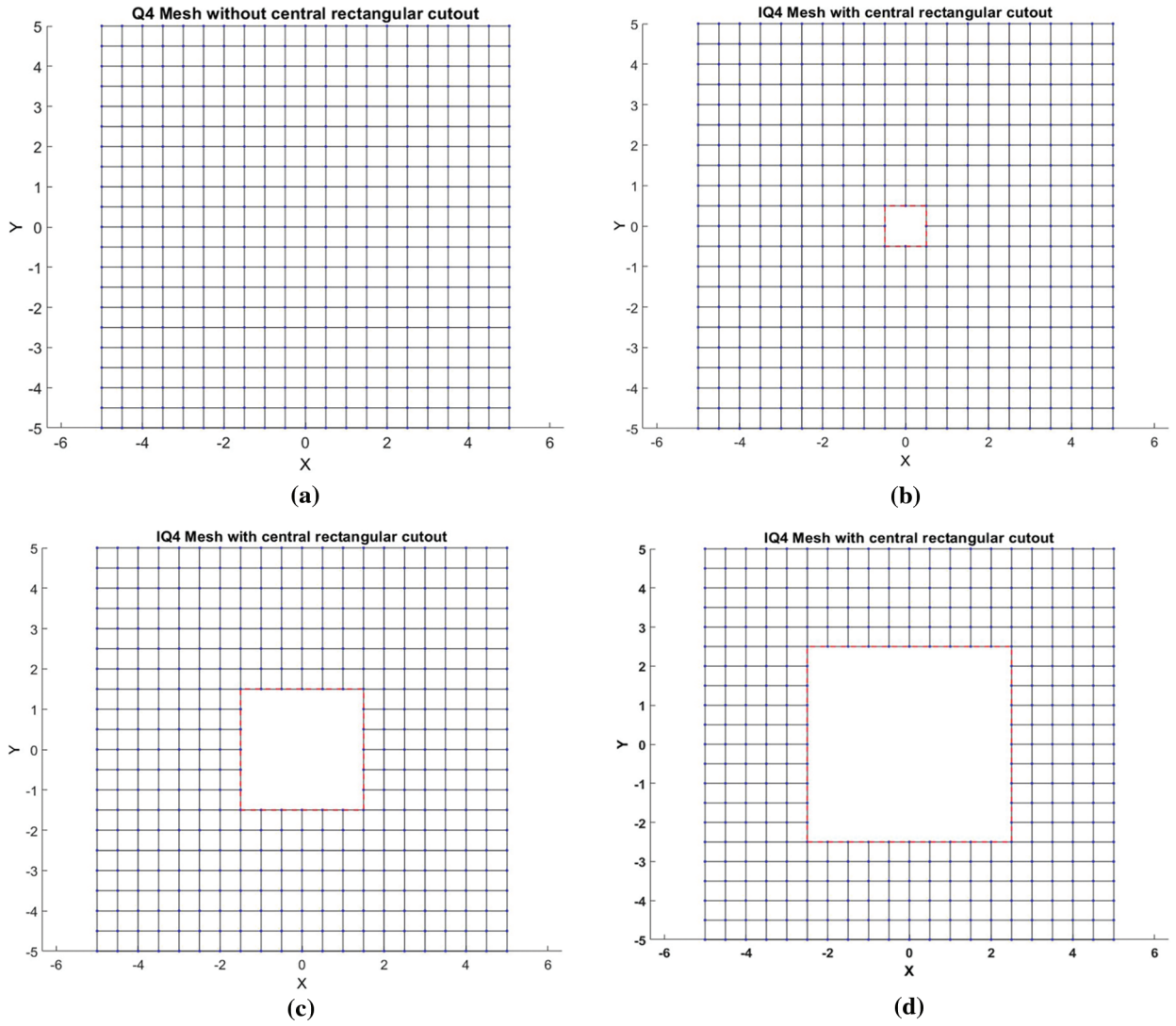

Figure 4: Finite element mesh and geometric configurations of simply supported square FG-CNTRC plates with central cutouts for various cutout aspect ratios: (**a**) FG-UD; (**b**) FG-O; (**c**) FG-X; (**d**) FG-V

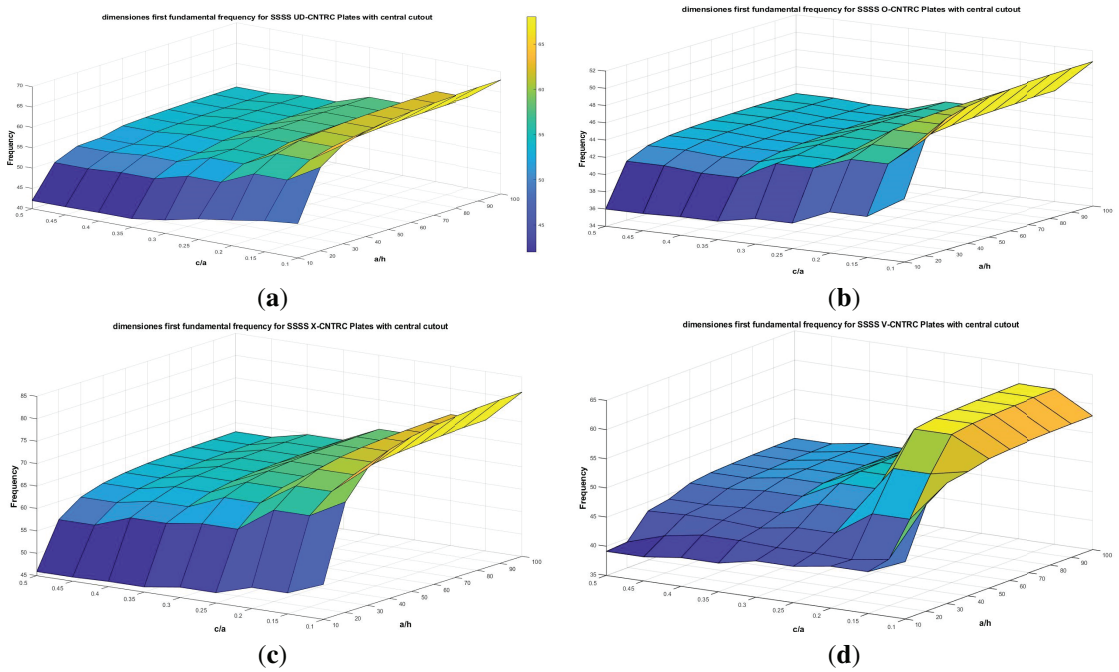

Figure 5: Variation of the first dimensionless natural frequency with respect to longitudinal (c/a) and transversal (d/b) cutout aspect ratios for different CNT distribution patterns: (**a**) FG-UD; (**b**) FG-O; (**c**) FG-X; (**d**) FG-A

4 Conclusion

In the present study, the free vibration characteristics of functionally graded carbon nanotube-reinforced composite (FG-CNTRC) plates with central cutouts have been thoroughly investigated by developing an improved finite element formulation. A novel IQ4γ element, based on the first-order shear deformation theory (FSDT), was implemented by incorporating an enhanced membrane formulation and a discrete shear projection technique. This improved formulation effectively eliminates shear locking and captures the membrane–bending coupling behavior, thereby extending the applicability of conventional FSDT-based plate elements to complex nanocomposite configurations. The accuracy and reliability of the proposed model were verified through systematic comparisons with benchmark results available in the literature. Subsequent parametric studies assessed the influence of CNT distribution profiles, cutout aspect ratios, and boundary conditions. The principal findings can be summarized as follows:

- The proposed IQ4 element demonstrated excellent performance in predicting natural frequencies of FG-CNTRC plates, particularly in capturing shear deformation and coupling effects, with reduced computational cost.
- Among the CNT distribution patterns, the FG-X configuration consistently yielded the highest natural frequencies due to the surface-concentrated reinforcement. At the same time, the FG-O layout resulted in the lowest frequencies due to mid-plane CNT concentration.
- The increase in longitudinal cutout aspect ratio (c/a) had a more significant effect on frequency reduction than the transverse ratio (d/b), especially in FG-O and FG-V configurations, highlighting the importance of axial stiffness in dynamic response.
- Larger cutout sizes were generally associated with decreased stiffness and reduced frequency values, with the FG-X layout exhibiting the most robust performance under increasing geometric discontinuities.

- The effect of boundary conditions was observed, where fully clamped plates exhibited higher frequencies than simply supported ones, due to enhanced edge constraints and stiffness.
- The study confirms that optimal CNT distribution, particularly surface-focused patterns like FG-X, combined with controlled cutout geometry, can significantly improve nanocomposite plates' dynamic performance in advanced engineering applications.

The developed computational model provides an accurate and efficient tool for the vibrational analysis of FG-CNTRC plates with geometric discontinuities. This study's findings are a useful reference for future investigations involving different cutout shapes, locations, and composite configurations, contributing to the structural optimization of high-performance materials in aerospace, mechanical, and civil engineering domains.

Acknowledgement: The authors thank all collaborators for contributing to this research.

Funding Statement: The authors received no specific funding for this study.

Author Contributions: The authors confirm contribution to the paper as follows: Conceptualization, Boudjema Bendaho and Zakaria Belabed; methodology, Zakaria Belabed; software, Abdelhak Mesbah; validation, Boudjema Bendaho, Abdelhak Mesbah, and Zakaria Belabed; formal analysis, Zakaria Belabed; investigation, Boudjema Bendaho; resources, Abdelhak Mesbah; data curation, Boudjema Bendaho; writing—original draft preparation, Boudjema Bendaho; writing—review and editing, Zakaria Belabed; visualization, Abdelhak Mesbah; supervision, Zakaria Belabed; project administration, Zakaria Belabed. All authors reviewed the results and approved the final version of the manuscript.

Availability of Data and Materials: The corresponding author can provide the datasets generated or analyzed during this study, upon a reasonable request.

Ethics Approval: The present work is purely computational/theoretical and did not require approval from an ethics committee, as no human or animal subjects were involved.

Conflicts of Interest: The authors declare no conflicts of interest to report regarding the present study.

References

1. Kalhori A, Bayat MJ, Asemi K. Buckling analysis of stiffened functionally graded multilayer graphene platelet reinforced composite plate with circular cutout embedded on elastic support subjected to in-plane normal and shear loads. Results Eng. 2023;20(6348):101563. doi:10.1016/j.rineng.2023.101563.
2. Singh D, Kiran R, Vaish R. Vibration and buckling analysis of agglomerated CNT composite plates via isogeometric analysis using non-polynomial shear deformation theory. Eur J Mech A. 2023;98(1):104892. doi:10.1016/j.euromechsol.2022.104892.
3. Kalgutkar AP, Banerjee S. Dynamic instability analysis of perforated stiffened laminated composite panels subjected to non-uniform in-plane edge load under hygrothermal condition. Thin Walled Struct. 2022;181(2):109961. doi:10.1016/j.tws.2022.109961.
4. Taibi N, Belabed Z, Boucham B, Benguediab M, Tounsi A, Khedher KM. On the thermomechanical behavior of laminated composite plates using different micromechanical-based models for coefficients of thermal expansion (CTE). J Appl Comput Mech. 2024;10(2):224–44. doi:10.22055/jacm.2023.44257.4191.
5. Guerine MHE, Belabed Z, Tounsi A, Mohamed SM, Althobaiti S, Selim MM. On the free vibration behavior of carbon nanotube reinforced nanocomposite shells: a novel integral higher order shear theory approach. Struct Eng Mech. 2024;91(1):1. doi:10.12989/sem.2024.91.1.001.
6. Ratankumar SV, Koteswara Rao L, Kiran Kumar M. Design of multi-valued logic circuit using carbon nano tube field transistors. Comput Mater Contin. 2022;73(3):5283–98. doi:10.32604/cmc.2022.027975.

7. Wang Y, Liu B, Zhu J, Zhou W, Jiang L, Pan C, et al. Thermal vibration of stiffened FGM plates with cutouts using Nitsche-based isogeometric approach. Thin Walled Struct. 2025;210(8):113026. doi:10.1016/j.tws.2025.113026.
8. Zeinali M, Rahimi G, Hosseini S. Buckling load optimization of sandwich plates with trapezoidal corrugated core and elliptical cutout using vibration correlation techniques and artificial neural network; experimental and numerical analysis. Thin Walled Struct. 2024;200(2):111957. doi:10.1016/j.tws.2024.111957.
9. Yu W, Guo R, Zhao Y, Chen M. Isogeometric flutter analysis of a heated laminated plate with and without cutout. Thin Walled Struct. 2025;206:112652. doi:10.1016/j.tws.2024.112652.
10. Dewangan HC, Panda SK, Sharma N. A review of linear and nonlinear structural responses of laminated flat/curved panels with and without cutout under thermo-mechanical loading. Compos Struct. 2023;303:116340. doi:10.1016/j.compstruct.2022.116340.
11. Fan F, Cai X, Sahmani S, Safaei B. Isogeometric thermal postbuckling analysis of porous FGM quasi-3D nanoplates having cutouts with different shapes based upon surface stress elasticity. Compos Struct. 2021;262(6):113604. doi:10.1016/j.compstruct.2021.113604.
12. Jana K, Pal S, Haldar S. Modal analysis of power law functionally graded material plates with rectangular cutouts. Mech Based Des Struct Mach. 2024;52(5):2411–39. doi:10.1080/15397734.2023.2180033.
13. Geng X, Zhao L, Zhou W. Finite-element buckling analysis of functionally graded GPL-reinforced composite plates with a circular hole. Mech Based Des Struct Mach. 2021;49(7):1028–44. doi:10.1080/15397734.2019.1707688.
14. Mirzaei M. Vibrations of FG-CNT reinforced composite cylindrical panels with cutout. Mech Based Des Struct Mach. 2022;50(1):79–99. doi:10.1080/15397734.2019.1705165.
15. Tran TT, Huong HTT. The nonlinear free vibration analysis-based an enhanced finite element procedure of tri-functionally graded sandwich plates with a square central cutout. Mech Based Des Struct Mach. 2025;53(5):3736–58. doi:10.1080/15397734.2024.2435567.
16. Prusty JK, Papazafeiropoulos G, Sahu DP, Mohanty SC. Free vibration analysis of sandwich shells with cutouts: an experimental and numerical study with artificial neural network modelling. Mech Adv Mater Struct. 2024;1–13. doi:10.1080/15376494.2024.2414412.
17. Ghadiri Rad MH, Hosseini SM. Application of the CUF-EFG method for buckling analysis of the multilayer GPLs–CNTs-reinforced FG plates with cutout. Mech Adv Mater Struct. 2024;31(3):533–49. doi:10.1080/15376494.2022.2116664.
18. Singh D, Gupta A. Effect of circular and elliptical cutouts on the free vibration analysis of sandwich FGM plate under the elastic foundations. Mech Based Des Struct Mach. 2025;53(3):2363–89. doi:10.1080/15397734.2024.2408604.
19. Shi S, Qi Y, Zhang C, Meng Q, Liu Y, Jin G, et al. In-plane vibration analysis of square plate with multiple cutouts. Shock Vib. 2021;2021(1):5540123. doi:10.1155/2021/5540123.
20. Zheng J, Zhang C, Khan A, Sebaey TA, Farouk N. On the asymmetric thermal stability of FGM annular plates reinforced with graphene nanoplatelets. Eng Comput. 2022;38(5):4569–81. doi:10.1007/s00366-021-01463-y.
21. Lee SY. Dynamic stability and nonlinear transient behaviors of CNT-reinforced fiber/polymer composite cylindrical panels with delamination around a cutout. Nonlinear Dyn. 2020;99(4):2551–69. doi:10.1007/s11071-020-05477-x.
22. Chen SX, Sahmani S, Safaei B. Size-dependent nonlinear bending behavior of porous FGM quasi-3D microplates with a central cutout based on nonlocal strain gradient isogeometric finite element modelling. Eng Comput. 2021;37(2):1657–78. doi:10.1007/s00366-021-01303-z.
23. Zeighami V, Jafari M. Stress analysis of perforated composite plates reinforced with carbon nanotubes with different distributions. Emergent Mater. 2021;4(6):1711–23. doi:10.1007/s42247-021-00191-9.
24. Shojaee T, Mohammadi B, Pourhosseinshahi M, Zeydabadi I. Buckling and post-buckling analysis of composite laminates with cutout under compressional loading based on the first-order shear deformation theory. Acta Mech. 2023;234(5):2145–65. doi:10.1007/s00707-023-03486-6.
25. Kumar R, Kumar R, Tiwari S, Hirwani CK. Finite element modelling and dynamic behavior analysis of sandwich panel with cutout. In: Polymer composites: from computational to experimental aspects. Singapore: Springer Nature; 2024. p. 287–311. doi:10.1007/978-981-97-0888-8_14.

26. Ansari R, Hassani R, Hasrati E, Rouhi H. Geometrically nonlinear vibrations of FG-GPLRC cylindrical panels with cutout based on HSDT and mixed formulation: a novel variational approach. Acta Mech. 2021;232(9):3417–39. doi:10.1007/s00707-021-03000-w.
27. Fazilati J, Khalafi V. Panel flutter analysis of perforated plate repaired by VSCL bonded patch using the multi-patch IGA approach. Thin Walled Struct. 2021;169(1):108465. doi:10.1016/j.tws.2021.108465.
28. Chand Dewangan H, Kumar Panda S, Kumar Hirwani C. Numerical deflection and stress prediction of cutout borne damaged composite flat/curved panel structure. Structures. 2021;31:660–70. doi:10.1016/j.istruc.2021.02.016.
29. Mohamed NA, Shanab RA, Eltaher MA, Abdelrahman AA. Vibration response of viscoelastic nanobeams including cutouts under moving load. Results Eng. 2023;20(5):101407. doi:10.1016/j.rineng.2023.101407.
30. Li Q, Huang W, Sanchez J, Wang P, Ding Q, Wang J. Free vibration analysis of rectangular plate with cutouts under elastic boundary conditions in independent coordinate coupling method. Comput Model Eng Sci. 2023;134(3):2093–121. doi:10.32604/cmes.2022.021340.
31. Mirzaei M, Kiani Y. Free vibration of functionally graded carbon-nanotube-reinforced composite plates with cutout. Beilstein J Nanotechnol. 2016;7:511–23. doi:10.3762/bjnano.7.45.
32. Al-Wesabi FN, Alsolai H, Mustafa Hilal A, Ahmed Hamza M, Al Duhayyim M, Negm N. Piezoresistive prediction of CNTs-embedded cement composites via machine learning approaches. Comput Mater Contin. 2022;71(1):1503–19. doi:10.32604/cmc.2022.020485.
33. Wang S, Li S, Zhai Z, Guo A, Qu P. Vibration characteristics of composite damping plate with randomly oriented carbon nanotube reinforced stiffeners. Int J Mech Mater Des. 2024;20(3):525–43. doi:10.1007/s10999-023-09689-y.
34. Zghal S, Dammak F. Functionally graded materials: analysis and applications to FGM, FG-CNTRC and FG Porous structures. Philadelphia, PA, USA: CRC Press; 2024. doi:10.1201/9781003483786.
35. Zghal S, Nasri R. Experimental investigation for forced vibration of honeycomb sandwich beams. In: Advances in acoustics and vibration. Berlin/Heidelberg, Germany: Springer; 2016. p. 223–33. doi:10.1007/978-3-319-41459-1_22.
36. Zghal S, Frikha A. Static behavior of carbon nanotubes reinforced functionally graded nanocomposite cylindrical panels. In: Design and modeling of mechanical systems—III. Berlin/Heidelberg, Germany: Springer; 2017. p. 199–207. doi:10.1007/978-3-319-66697-6_20.
37. Hadrich A, Zghal S, Koubaa S, Bouaziz Z. Free vibration of functionally graded porous perforated solid structures with complex shaped holes. Int J Solids Struct. 2025;319(3):113449. doi:10.1016/j.ijsolstr.2025.113449.
38. Tornabene F, Viscoti M, Dimitri R. Free vibration analysis of laminated anisotropic doubly-curved shell structures reinforced with three-phase polymer/CNT/fiber material. Eng Anal Bound Elem. 2024;164:105762. doi:10.1016/j.enganabound.2024.105762.
39. Wang S, Zheng C, Li S, Guo A, Qu P, Hu Y. Free vibration of functionally graded carbon nanotube-reinforced composite damping structure based on the higher-order shear deformation theory. Polym Compos. 2023;44(2):873–85. doi:10.1002/pc.27138.
40. Masoodi AR, Ghandehari MA, Tornabene F, Dimitri R. Natural frequency response of FG-CNT coupled curved beams in thermal conditions. Appl Sci. 2024;14(2):687. doi:10.3390/app14020687.
41. Seyfi A, Teimouri A, Dimitri R, Tornabene F. Dispersion of elastic waves in functionally graded CNTs-reinforced composite beams. Appl Sci. 2022;12(8):3852. doi:10.3390/app12083852.
42. Akhila G, Natarajan S, Lian H, Katili I. Locking-free polygonal plate element based on the discrete shear projection method. Comput Struct. 2025;309:107661. doi:10.1016/j.compstruc.2025.107661.
43. Makarim Katili A, Bletzinger KU, Katili I. An enrichment of Q4γ plate finite element using incomplete quadratic functions, an assumed energy orthogonality of Bergan's free formulation, and mixed transverse shear strains. Comput Struct. 2025;307:107619. doi:10.1016/j.compstruc.2024.107619.

44. Belabed Z. A new application of quadrilateral finite element model incorporating the discrete shear projection technique for free vibration response of CNT reinforced plates. Int J Solids Struct. 2025;309(23):113204. doi:10.1016/j.ijsolstr.2024.113204.
45. Batoz JL, Katili I, Widyatmoko S, Antaluca E. An efficient shear and bending-locking-free quadrilateral plate element using a modified Hellinger-Reissner functional and the Bergan free formulation. Int J Numer Meth Eng. 2024;125(12):e7451. doi:10.1002/nme.7451.